Surface Science 719 (2022) 122041

Contents lists available at ScienceDirect

Surface Science

journal homepage: www.elsevier.com/locate/susc

Monte Carlo simulations of the self-assembly of hierarchically organized metal-organic networks on solid surfaces

Karolina Nieckarz [a], Paweł Szabelski [b], Damian Nieckarz [b,*]

[a] Faculty of Chemistry, Maria Curie-Skłodowska University in Lublin, Maria Curie-Skłodowska Square 3, 20-031 Lublin, Poland
[b] Department of Theoretical Chemistry, Institute of Chemical Sciences, Faculty of Chemistry, Maria Curie-Skłodowska University in Lublin, Maria Curie-Skłodowska Square 3, 20-031 Lublin, Poland

ARTICLE INFO

Keywords:
Self-assembly
Monte Carlo simulations
Hierarchically organized overlayers
Metal-organic networks
Adsorption
Chirality

ABSTRACT

The coordination-driven self-assembly of two-dimensional (2D) supramolecular architectures is a convenient method of rational construction of one-atom-thick nanomaterials with desired topology, intriguing physicochemical properties and high cognitive value. In this work, we use coarse-grained Monte Carlo (MC) computer simulations to study the self-assembly of functional bridging ligands with mononuclear metal centers on a triangular lattice. Particularly, we focus on the role of anisotropic, reversible ligand → metal coordinate bonds in the bottom-up formation of hierarchically organized metal-organic networks composed of star-shaped and rod-like linkers (representing real organic molecules) and trivalent metal atoms. In our model π aromatic ligands were modeled in a simplified way as a collection of flat, rigid, and interconnected segments with properly encoded short-ranged interactions. Depending on the composition of the investigated overlayers, we observed the spontaneous formation a cascade of openwork (co)crystals with a hierarchical structure, controllable chirality and scalable morphological properties like porosity, connectivity, density, etc. Our theoretical findings can pave the way for the experimental fabrication of the novel surface-confined metal-organic networks (SMONs) in which anisotropic coordinate bonds play a decisive role.

1. Introduction

The rational synthesis of low-dimensional surface-confined metal-organic networks (SMONs) with programmable spatial structure, tuneable composition and intriguing physicochemical properties is nowadays a research hotspot in materials science [1–3]. Such atomically thin self-assembled nanomaterials usually exhibit a highly periodic arrangement of empty voids (differing in size, shape and chirality), bridging ligands (usually simple carbon-based molecules) and mono- [4–6] or multinuclear metal centers [7,8]. In the nanoporous SMONs the spatially separated and locked into precisely defined positions metal atoms serve as well-defined connecting points for appropriately functionalized (bi-, tri-, or polydentate) π aromatic ligands [4,6,9,10]. Contrary to the bulk phase, at atomically flat metallic substrates most d- and f-block transition metals can accommodate from 2 to 6 sterically undemanding ligands (with small cone angle) equipped with terminal donor atoms [6] or identical electronegative centers like nitrile moiety (-C ≡ N) [4,11], propiolonitrile functional group (-C ≡ C-C ≡ N) [12], hydroxyl group (-OH) [13], and others [14,15]. Among the above mentioned planar coordination complexes those with linear (ligand → metal ← ligand) [16], trigonal [4,17], and square geometry [18] are usually seen. Such surface-supported metal-organic nodes are energetically stabilized not only by the anisotropic ligand → metal coordinate bonds (dative covalent bonds), but also by the presence of well-ordered solid surfaces. Therefore, the isolated metal centers embedded within the crystalline SMONs are not labile and easily accessible to guest atoms/molecules, what makes possible exploiting them in a selective adsorption [19] or as active centers of artificial metalloenzymes in a heterogeneous catalysis [20]. On the other hand, empty voids of structurally programmed SMONs may provide nanoscale spatial confinement for laterally interacting species [21], play the role of anchoring points for (macro)molecules in the interfacial host-guest chemistry (positioning of organic species), and capture of small molecules with complementary chirality and geometrical features [22]. Importantly, the metal-assisted self-assembly (and final topology) of periodic metal-organic networks can be reliably traced using non-destructive techniques, like non-contact atomic force microscopy (nc-AFM) [23] and low temperature scanning tunneling microscopy (STM) [24], which

* Corresponding author. D. Nieckarz, Phone: +48 081 537 56 92; Fax: +48 081 537 56 85
E-mail address: damian.nieckarz@poczta.umcs.lublin.pl (D. Nieckarz).

https://doi.org/10.1016/j.susc.2022.122041
Received 26 November 2021; Received in revised form 24 January 2022; Accepted 25 January 2022
Available online 31 January 2022

makes the interpretation of their structural properties straightforward and credible. As it has been demonstrated in numerous experimental studies, by a careful manipulating size, shape, and atomic structure of simple molecular building blocks it is possible to obtain plethora of diverse low-dimensional nanoarchitectures like open porous networks [6,17,25], quasicrystals [26], fractal crystals [27,28], chains [29], nanoribbons [30], ladders [31], large-sized macrocycles [32], small aggregates [33], and others [34]. However, the on-surface construction of hierarchically organized SMONs with programmable morphological properties and functions is extremely challenging from the scientific point of view. So far, the experimental efforts in this field were made only by Liu et al., who demonstrated that, on an atomically flat Au(111) surface, the self-assembly of star-shaped 1,3,5-tris(pyridyl)benzene ligands (TPyB) with Cu atoms can lead to the formation of partially ordered metal-organic networks with a hierarchical structure [35]. In this context, the rational construction of extended, defect-free, and multilevel SMONs with tailorable morphological properties still remains largely unexplored. Interestingly, in the recent years, a lot of flower-like 2D molecular assemblies, sustained by weak noncovalent interactions, were prepared experimentally at interfaces. Among them are monocomponent overlayers comprising simple, highly symmetrical molecules, like the trimesic acid (TMA) [36], functionalized hexaphenylbenzene (HPB) [37], methyltrioxatriangulenium (Me-TOTA) [38], 2,4,6-tris(2-pyridyl)-1,3,5-triazine (TPTZ) [39] and the others [40–42]; bicomponent porous networks [43], and even trinary supramolecular architectures with global organizational chirality [44]. Inspired by the above listed scientific reports we have focused recently on the possibility of computer-aided design of analogous multi-walled SMONs with high structural complexity. For this purpose, we selected lattice Monte Carlo (MC) computer simulations, recognized as reliable and efficient tool in the surface nanostructure formation predictions in the past decade [45–47]. Next, we constructed coarse-grained theoretical model in which real π aromatic ligands (and metal atoms) are mapped into flat triangular lattice maintaining their most vital structural properties intact (size, shape, number and intramolecular distribution of active interaction centers). With this approach it was possible a comprehensive examination of complex metal-organic overlayers (composed of up to two thousands of individual components) with the use of only a few adjustable parameters like surface coverage θ, linear size L of the 2D simulation box, temperature T, ligand → metal coordination bond energy ω, etc. Initially, we ran the preliminary MC computer simulations for the two-component metal-organic mixtures comprising rod-like/star-shaped linkers and trivalent metal atoms. Next, a series of predictive MC calculations were performed for the analogous three-component overlayers composed of trivalent metal atoms and bridging linkers differing in size, shape and functionalization. To our surprise, it turned out that the metal-directed coassembly of archetypical π aromatic ligands (used so far routinely in the experimental fabrication of homoporous metal-organic networks at surfaces) can result in the formation a series of unreported so far flower-like SMONs with controllable chirality and scalable morphological properties like composition, porosity, connectivity, etc. The obtained theoretically 2D (co)crystals were structurally analyzed in detail and described quantitatively using a parameter further called structural index $n \in N$. Moreover, their high structural coherence was confirmed by the metal-metal radial distribution function $g(r)$ calculations. All these informations can be valuable in the context of rational designing new supramolecular architectures with tailorable adsorptive and catalytic properties on solid surfaces.

2. The model

To investigate the self-assembly of surface-confined metal-organic networks, we have performed a series of lattice Monte Carlo (MC) computer simulations in the *NVT* ensemble, where N stands for the total number of components present in the 2D simulation box, V means its volume (surface area) and T temperature. Namely, MC numerical calculations were performed on a rhombic fragment of the triangular lattice at fixed surface coverage $\theta = \sigma(L)L^{-2}$, defined as the product of occupied adsorption sites $\sigma(L)$ on a triangular lattice with linear size $L = 120$, and inverse of the total number of adsorption sites L^2 in the investigated system. To provide optimal conditions for unperturbed self-assembly of 2D supramolecular patterns, the MC simulations were conducted under low surface coverage $\theta \sim 0.23$. In our coarse-grained model the flat triangular lattice (appropriately scaled square grid) is composed of evenly distributed vertices (adsorption sites), and represents the smooth, defect-free (no kinks, edges, terraces, etc.) and energetically homogeneous metallic surface with (111) geometry like Cu(111), Ag(111), or Au(111). For convenience, the distance between two adjacent adsorption sites on a triangular lattice was set to 1 and expressed in dimensionless units. Additionally, to eliminate the negative edge effects resulting from the finite size of the investigated systems, standard periodic boundary conditions were imposed on a triangular lattice in all directions. As it is seen in Fig. 1, the functionalized π aromatic ligands (denoted as **A, B**, and **C**, respectively) were modeled on a triangular lattice in a simplified way, as flat linkers composed of rigid interconnected segments (hard spheres). In this representation each linker's segment corresponds to individual aromatic ring of real molecule **A-C**, and occupies one adsorption site on a triangular lattice (localized monolayer adsorption). Analogously, the connections between individual rigid segments building the simulated ligands represent C−C σ-bonds of real aromatic molecules **A-C**. Moreover, the arm's ends (terminal segments) of the investigated linkers were equipped with anisotropic interaction centers playing the roles of *para/meta* electronegative functional groups present in the tested molecules (see bottom panel in Fig. 1). The trivalent metal atoms **M** (**M** = Fe, Co, Ni, Cu or Ce) were modeled in a very similar way - as single, isolated segments with appropriately assigned interaction directions on a triangular lattice. To examine the metal-assisted self-assembly of supramolecular architectures we assumed that the terminal interaction centers of bridging linkers **A-C** are able to form attractive coordinate bonds with coadsorbed metal atoms. Additionally, the ligand → metal coordinate bonds were assumed to be highly directional, short-ranged (limited to the adjacent adsorption sites on a triangular lattice) and reversible. Therefore, a single anisotropic coordinate bond with energy $\omega = -1.0$ (negative value means attraction) was allowed to form only when a linker molecule (connector) and metal atom **M** met in a proper planar configuration on a triangular lattice, and interaction directions assigned to them were collinear and oppositely directed (→ ←). In order to emphasize the dominant role of ligand → metal coordinate bonds in the bottom-up formation of ordered SMONs, all other possible lateral interactions (metal↔metal, linker↔linker, etc.) between the components of the simulated overlayers were neglected for the sake of simplicity. The same refers to the linker(metal)↔triangular lattice interactions whose energy was set equal to zero.

As it is seen in Fig. 1, the simplest chemical structure corresponds to the C_2-symmetric molecule **A**, which is composed of two collinear aromatic rings connected by a single σ-bond. Each aromatic ring of the achiral ligand **A** is equipped with a well-defined interaction center G embedded at *para* position. The very similar distribution of terminal active centers (functional groups) also characterize the C_3-symmetric connector **B**, comprising four interconnected segments - central inactive core (1,3,5-substituted benzene ring) plus three arm segments (*para*-functionalized phenyl moieties). Contrary to the achiral molecules **A** and **B**, which adopt a unique conformation when adsorbed, the star-shaped ligand **C** (constitutional isomer of molecule **B**) is conformationally flexible due to rotatability of the outer phenyl rings around individual C−C σ-bonds. Therefore, the *meta*-functionalized linker **C** is prochiral (achiral in the bulk phase but chiral under 2D confinement), and upon adsorption at the solid surface can adopt one of the four distinct conformations, denoted arbitrary as (*rrr*)**C**, (*rrs*)**C**, (*srr*)**C**, and (*sss*)**C** (see Fig. 1). Among them are both C_{3h}-symmetrical surface enantiomers (*rrr*)

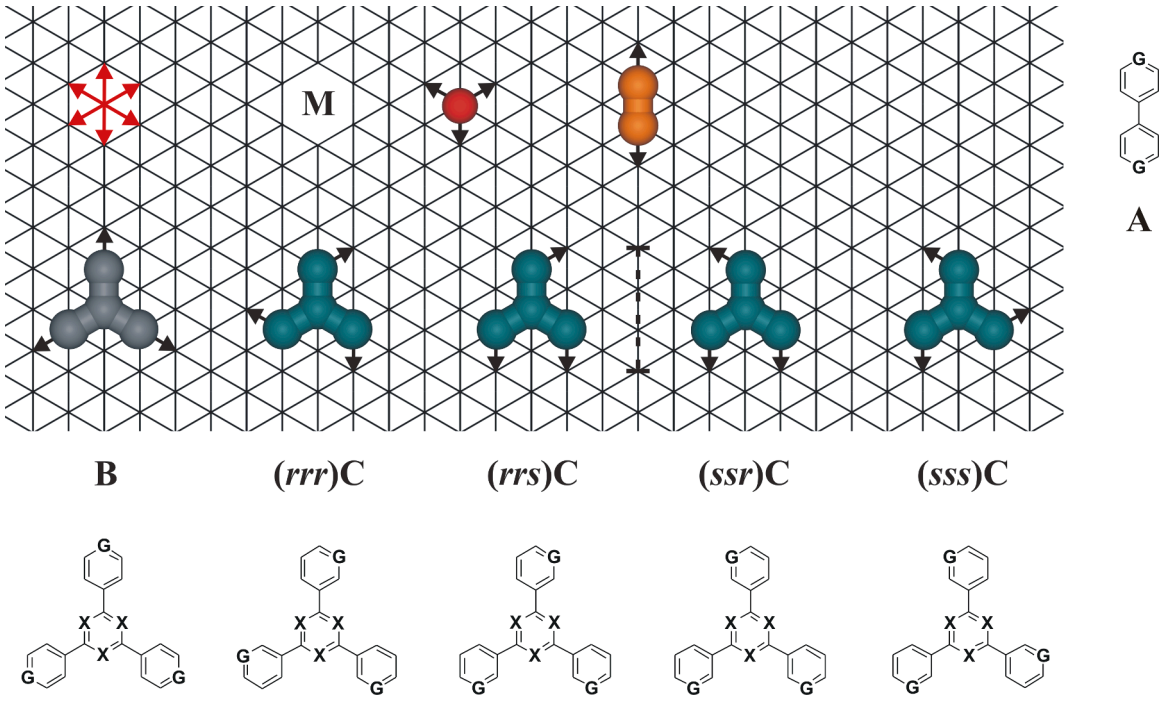

Fig. 1. Mapping of trivalent metal atom **M** (red isolated segment, **M** = Fe, Co, Ni, Cu or Ce) and archetypical π aromatic ligands **A, B**, and **C** (X = C, N) on a 2D triangular lattice. Letters G denote positions of distinct electronegative centers like nitrile moiety (-C ☰ N), propiolonitrile functional group (-C ☰ C-C ☰ N) or ring-nitrogen atom (-N:) within presented molecules. The black arrows indicate in-plane interaction directions assigned both to the terminal segments of the modeled ligands **A-C** and trivalent metal atom **M**. The dashed line represents mirror plane for the surface conformers of prochiral ligand **C** (turquoise tripods). The intersecting red arrows mark the directions of a triangular lattice.

C | (*sss*)**C** and mirror-image conformers (*rrs*)**C** | (*srr*)**C** with C_s symmetry.

The custom source codes of lattice MC simulations were written in Fortran 95 programming language and run in a free Linux environment. Specifically, the applied simulation algorithm can be outlined as follow. Initially, all components of the simulated overlayers (metal atoms and bridging linkers) were distributed randomly on a triangular lattice in a preselected stoichiometric ratio. Next, to bring the modeled assemblies into a thermodynamic equilibrium 10^{10}, MC steps (MCs) were performed (one MCs is a single attempt of a lateral displacement and/or rotation of a randomly selected entity from the adsorbed overlayer). Namely, the randomly chosen linker/metal atom was removed from its old position Ω on a triangular lattice. Then, the coordinates of the Ω′ set (comprising one, two or four adjacent adsorption sites arranged in a shape corresponding to the removed entity), were determined using pseudo-random numbers. If the Ω′ set (trial position) was empty ($\Omega' = \varnothing$), the linker/metal atom was placed in the trial position on a triangular lattice. Otherwise ($\Omega' \neq \varnothing$), the selected entity was left in the old position Ω, and the above described procedure was successively iterated. The transition probability $P(\Omega \rightarrow \Omega')$ was calculated based on the classical Metropolis criterion $P(\Omega \rightarrow \Omega') = min\{1, exp(-\Delta E/k_BT)\}$ [48], where $\Delta E = E_{\Omega'} - E_{\Omega}$ is the potential energy difference between the trial and the old state, k_B denotes Boltzmann constant ($k_B = 1$ in our model) and T is the system temperature. If the total potential energy of randomly selected linker/metal atom in a trial position Ω′ was lower or equal to its total potential energy in the old state (that is $E_{\Omega'} \leq E_{\Omega}$), the trial position Ω′ was accepted unconditionally and became a new configuration Ω* of the probed entity ($\Omega' \rightarrow \Omega^*$). Otherwise, the pseudo-random number $r \in (0, 1)$ was generated and compared with the exponential factor $exp(-\Delta E/k_BT)$. If the pseudo-random number r satisfied inequality $r \leq exp(-\Delta E/k_BT)$, the Ω′ position was accepted ($\Omega' \rightarrow \Omega^*$). In the opposite case, the trial position Ω′ was discarded ($\Omega' \rightarrow \Omega$). After 10^{10} MCs performed at fixed temperature ($T = 0.16$), the investigated adsorbed overlayer was linearly cooled down to the low, target temperature $T = 0.01$ (10^4 MCs per temperature interval $dT = 0.01$) and structurally analyzed in detail. The additional annealing procedure was applied to heal sparse point defects (missing linkers/metal atoms) of assembled metal-organic networks and finally improve their structural integrity. The energies and temperature in our theoretical model are reduced quantities expressed in units of ω and $|\omega|/k_B$, respectively.

3. Results and discussion

3.1. Homoporous metal-organic networks

The preliminary MC simulations were carried out for a metal-organic overlayer composed of 1238 rod-like linkers **A** and 825 trivalent metal atoms **M** in a ∼ 3 : 2 stoichiometric ratio, which is optimal for the growth of extended 2D nanomeshes comprising bidentate organic ligands with linear backbone and d-block transition metal atoms like Co [4,17,49], Cu [21, 50], and Ce [7]. As it is seen in Fig. 2a, the rod-like bridging linkers **A** self-assembled with trivalent metal atoms into a defect-free, long-range ordered homoporous network (denoted as F_1), composed of empty hexagonal cavities α (highlighted in orange in Fig. 2). Each complete nanopore α has diameter $d = 6$ (metal-to-metal), includes 19 free adsorption sites and is surrounded by alternately arranged linkers **A** and metal atoms. The crystalline overlayer is characterized by a rhombic unit cell ($3\sqrt{3} \times 3\sqrt{3}$, $\angle = 60/120^{o}$), and has density equal to $\rho_1 = 0.342$ (expressed in the number of occupied lattice sites per unit cell area). Moreover, the coordinatively saturated metal atoms in the simulated phase create a 6^3 (6.6.6 in the expanded vertex notation) 1-uniform tessellation. As shown in the magnified fragment of a honeycomb-like network, the hexagonal tiling is defined by a vertex (marked by a single black dot) surrounded by three regular hexagons connected edge-to-edge and vertex-to-vertex in the Euclidean plane. Within the discussed overlayer, the C_3-symmetrical mononuclear coordination nodes $\mathbf{A_3M}$ are linked together by bifunctional bridging linkers **A** and exhibit a two-fold rotational degeneracy on a triangular lattice. As shown in the top-right inset in Fig. 2, the angles between rod-like

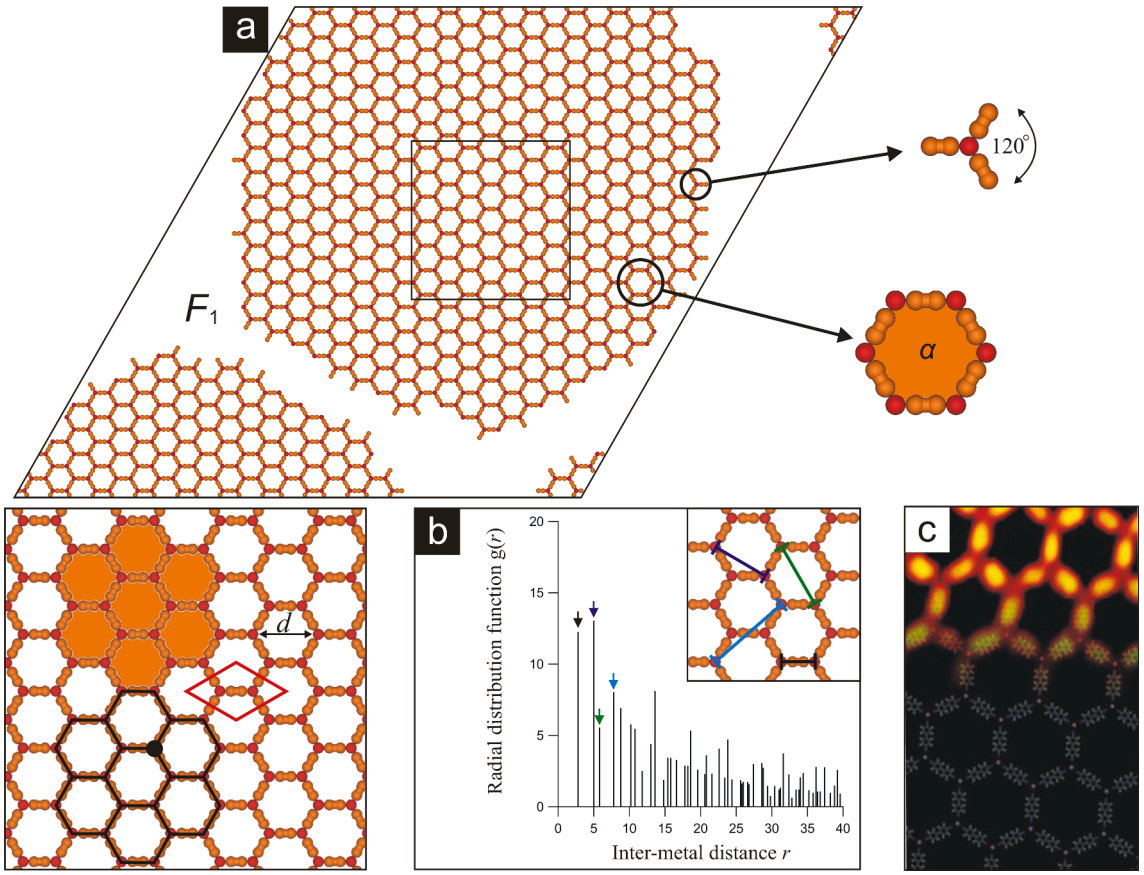

Fig. 2. (a) Snapshot of the simulated metal-organic overlayer comprising 1238 rod-like linkers **A** and 825 trivalent metal atoms **M** (red circles) in a $\sim$ 3 : 2 stoichiometric at surface coverage $\theta \sim 0.23$ and temperature $T = 0.01$. In the magnified fragment of the homoporous network (bottom-left panel), the rhombic unit cell is marked (solid red lines). The solid black lines connecting neighboring metal atoms represent small fragment of 6.6.6 regular tessellation, while the single black dot indicates defining vertex point. Hexagonal nanopores α with diameter $d = 6$ (metal-to-metal) are marked in an orange color. In the top-right insets the magnified coordination node $\mathbf{A_3M}$ and single nanopore α are shown. (b) Metal-metal radial distribution function $g(r)$ calculated for the single-walled network F_1 at temperature $T = 0.01$. Selected intermetallic distances **M↔M** are marked with different colors (black, purple, green, and light blue) and correspond to the individual peaks of the metal-metal radial distribution function (color arrows). (c) The high-resolution STM image of a nanoporous coordination network comprising [1,1′-biphenyl]-4,4′-dicarbonitrile ligands and Cu metal adatoms on the Cu(111) surface with partially superimposed DFT model. Reprinted (adapted) with permission from Ref. 50. Copyright (2017) American Chemical Society.

molecules **A** pointed to the single metal atom in a coordination motif $\mathbf{A_3M}$ are equal to 120°. The high symmetry of such planar complexes facilitates error correction during the nucleation and growth of a modeled overlayer. Importantly, the infinite metal-organic phase F_1 is isostructural with the 2D coordination network obtained experimentally recently by Cai et al. [50] (see Fig. 2c). Moreover its high structural coherence is confirmed by the metal-metal radial distribution function $g(r)$ calculations (see the section 2. of Supplementary Data for definition). As it follows from Fig. 2b the metal-metal radial distribution function $g(r)$ comprise a series of distinct peaks corresponding to the subsequent coordination shells of the superstructure F_1. The selected sharp peaks at distances $r < 10$ (expressed in the lattice spacing units) are marked with color arrows and linked with the appropriate intermetallic distances **M↔M** (top-right inset in Fig. 2b).

In the case of star-shaped linkers **B** mixed with trivalent metal atoms **M** in a stoichiometric ratio 1: 1, we observed spontaneous formation of perfectly ordered metal-organic network (denoted as F_∞) with a rhombic unit cell ($2\sqrt{3} \times 2\sqrt{3}$, $\angle = 60/120^o$) and density $\rho_\infty = 0.481$ [51] (see Fig. 3a). The homoporous adsorbed overlayer is composed of periodically distributed cavities β (7 adsorption sites), with diameter $d = 4$ (corner-to-corner). The coordinatively saturated metal atoms incorporated into superstructure F_∞ are arranged into a 3^6 (3.3.3.3.3.3 in the expanded vertex notation) 1-uniform (regular) tessellation and constitute isolated connecting points for the *para*-functionalized arms of unioriented molecules **B**. The above described topological features of infinite phase F_∞ match perfectly with structural properties of real 2D metal-organic assemblies prepared on the Ag(111) [52] and Au(111) [53] single-crystal surfaces, which confirms the correctness of the proposed theoretical model.

The individual surface enantiomers of the star-shaped linker **C** (and their racemic mixtures) were investigated in our previous studies [51, 54]. However, the coassembly of all surface conformers of a tritopic molecule **C** with trivalent metal atoms **M** was not tested so far theoretically or experimentally. Therefore, in this contribution, we modeled the *meta*-functionalized ligand **C** as a conformationally flexible connector. For this purpose, we assumed that the single coordination bond **C** → **M** can be formed only when the metal atom occupies adsorption site neighboring with one of the two *meta* positions of terminal segment (arm) of molecule **C**, and the adsorption site adherent to the second *meta* position of the same segment is not occupied by another metal atom. In this way, only one *meta* interaction center per terminal segment of molecule **C** is allowed. Therefore, the stochastic formation/dissociation of planar coordination motifs **C** → **M** differing in geometry is not biased by the fixed stoichiometric ratio between individual surface conformers of prochiral ligand **C**. As shown in Fig. 3b the mixture of prochiral linkers **C** and trivalent metal atoms **M** self-assembled into (R)-chiral metal-organic superstructure (denoted as F'_∞) with a small rhombic unit cell (3×3, $\angle = 60/120^o$), relatively high density $\rho'_\infty = 0.646$ and

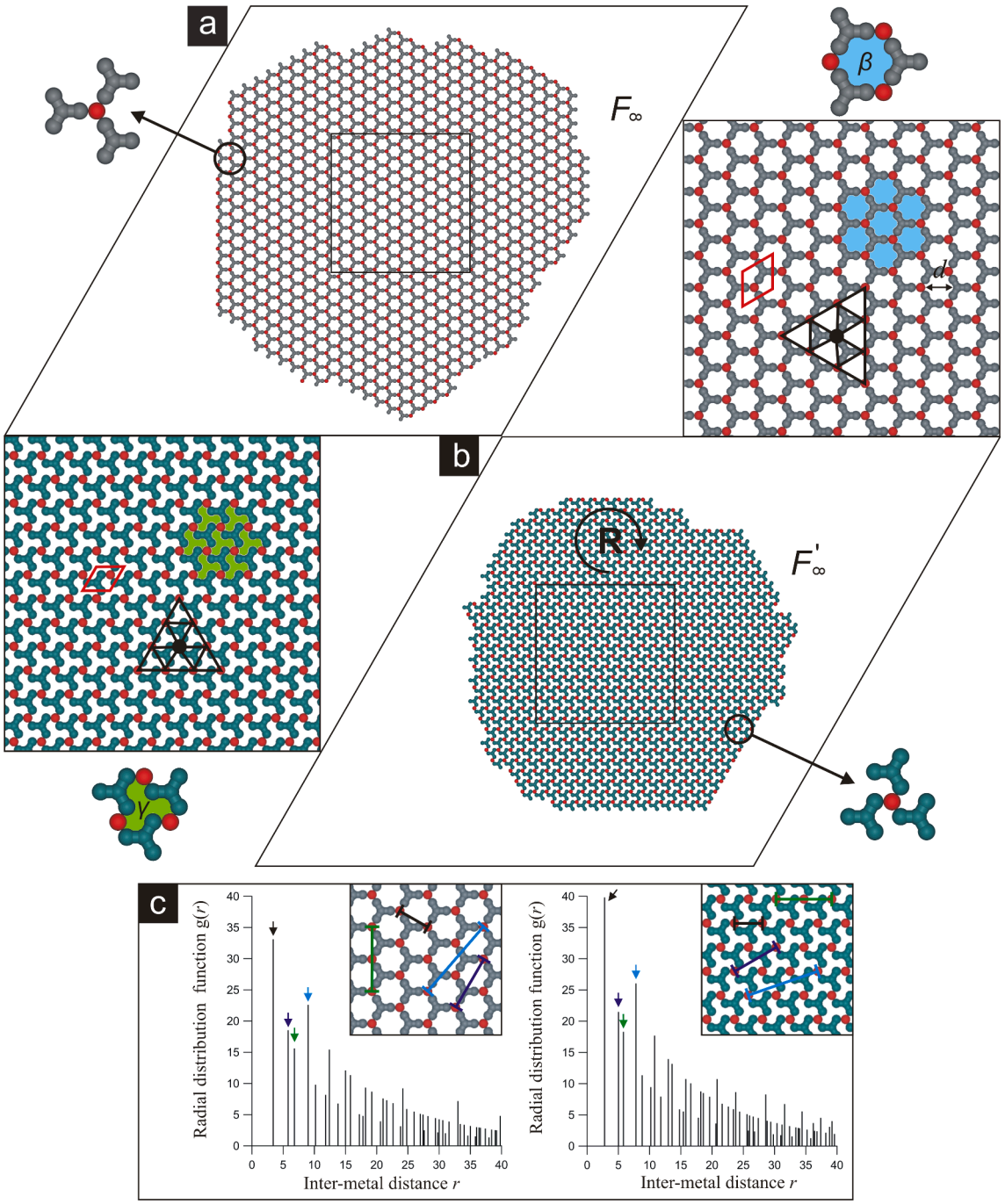

Fig. 3. A representative snapshots of the metal-organic networks composed of star-shaped linkers and trivalent metal atoms **M** (red segments). (a) Achiral supramolecular phase F_∞ comprising 660 linkers **B** (gray tripods) and 660 trivalent metal atoms **M** in a 1:1 stoichiometric ratio. (b) (R)-chiral overlayer F'_∞ comprising 660 prochiral linkers **C** (turquoise tripods) and 660 trivalent metal atoms **M** in a 1: 1 stoichiometric ratio. In the magnified fragments of the homoporous networks, the rhombic unit cells are marked (solid red lines). The solid black lines connecting neighboring metal atoms represent small fragments of 3.3.3.3.3.3 1-uniform tessellations, while the black dots indicate defining vertex points. The empty nanopores β and γ are marked in light blue and pale green color, respectively. In the top-left and bottom-right insets the magnified coordination nodes $\mathbf{B}_3\mathbf{M}$ and (*rrr*)$\mathbf{C}_3\mathbf{M}$ are shown. (c) Radial distribution functions $g(r)$ calculated for the homoporous networks F_∞ and F'_∞ at temperature $T = 0.01$. Selected intermetallic distances **M**↔**M** are marked with different colors (black, purple, green, and light blue) and correspond to the individual peaks (metal-metal coordination shells) of the metal-metal radial distribution functions (color arrows).

uniformly distributed star-shaped nanopores γ (4 free adsorption sites). Interestingly, the homochiral network F'_∞ is selectively built of windmill-like conformers (*rrr*)**C** (analogous phase with the opposite chirality is shown in Fig. S1 of the Supplementary Data). Indeed, in the studied system, there is a factor inhibiting formation of mixed coordination nodes comprising different conformers of *meta*-functionalized molecule **C**. The closer inspection of intramolecular distribution of active centers within the surface enantiomers (*rrs*)**C** | (*srr*)**C** unravel that the above mentioned factor is a steric effect. Namely, two out of three active centers of the mirror-image conformers (*rrs*)**C** | (*srr*)**C**, are parallel oriented (↓↓) and located to close each other to form the coordinatively saturated complex with a trivalent metal atom. Therefore, the metal-assisted chiral self-sorting occurring in the systems comprising different surface conformers of prochiral molecule **C** and trivalent metal

atoms **M** is very effective and results in the selective formation of homochiral metal-organic domain shown in Fig. 3b. Interestingly, the peak pattern corresponding to metal-metal radial distribution function $g(r)$ calculated for the (R)-chiral metal-organic network F'_{∞} is very similar like those determined for infinite overlayer F_{∞} (see Fig. 3c). However, the individual peaks at distances $r < 10$ are more intense, as compared to an achiral phase F_{∞}, indicating denser packing of the homoporous network F'_{∞} ($\rho'_{\infty} = 1.34\rho_{\infty}$).

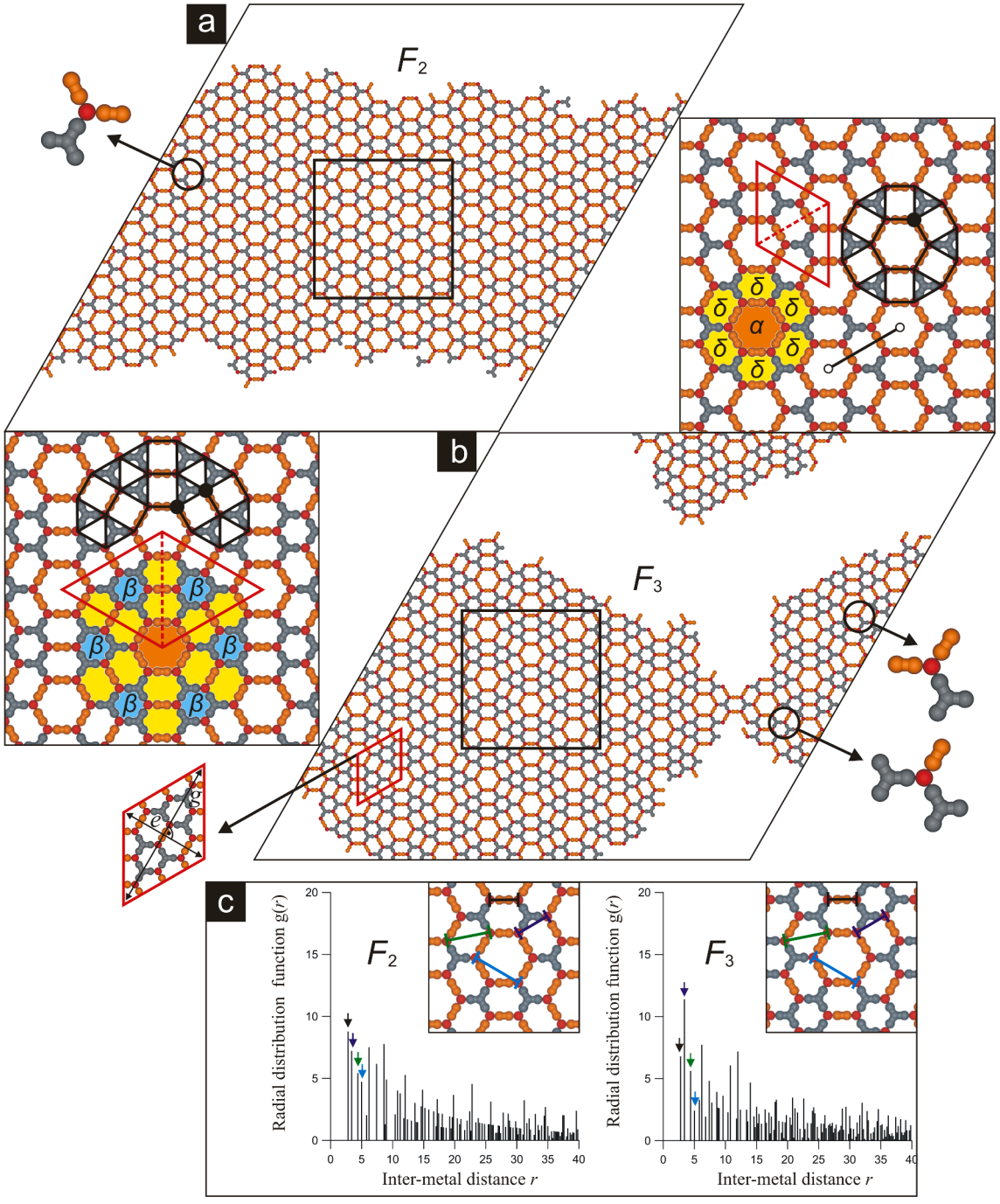

Fig. 4. (a) A representative snapshot of the achiral metal-organic network F_2 comprising 762 molecules **A**, 254 molecules **B** and 762 trivalent metal atom **M** in a 3: 1: 3 stoichiometric ratio. (b) The flower-like phase F_3 comprising 550 molecules **A**, 368 molecules **B** and 734 trivalent metal atoms **M** in a ~ 3 : 2 : 4 stoichiometric ratio. In the magnified fragments of the heteroporous networks, the rhombic unit cells are marked (solid red lines). The dashed red lines delimit triangular half-unit cells. The periodicity of the hierarchically organized phases is highlighted by the differently colored nanopores: α (orange color), β (light blue color) and δ (yellow color). The solid black lines connecting the neighboring metal atoms in the magnified fragments of the multi-walled networks represent small fragments of the irregular 1-uniform 3.4.6.4 and the irregular 2-uniform $3.4.6.4$; $3^3.4^2$ tessellation, while the black dots indicate defining vertex points. The black line segment (◯ – ◯) connects the centers of the adjacent hexagonal pores α in the supramolecular phase F_2. (c) Comparison of the metal-metal radial distribution functions $g(r)$ calculated for the successive networks F_2 and F_3 at temperature $T = 0.01$. Selected intermetallic distances **M**↔**M** are marked with different colors (black, purple, green, and light blue) and correspond to the individual peaks (metal-metal coordination shells) of the determined metal-metal radial distribution functions (color arrows).

3.2. Achiral heteroporous metal-organic networks

In this section, we are presenting the results of the predictive MC simulations devoted to surface-confined assemblies composed of rod-like and star-shaped linkers (**A** and **B**) coadsorbed with trivalent metal atoms **M** on the triangular lattice. Interestingly, in such overlayers, we observed spontaneous formation a family of highly periodic 2D networks with a hierarchical structure (see Figs. 4, 5, and 6a). In order to describe the obtained cocrystals quantitatively, we introduced a parameter called the structural index$n \in N$, corresponding to the total number of equidistant ligands **A** (**A**↔**A** $= 2\sqrt{3}$), perpendicular to the line segment ◯ − ◯ connecting the centers of the neighboring hexagonal nanopores α. As it is shown in Fig. 4a, the ordered superstructure F_2 ($\rho_2 = 0.400$) is characterized by a rhombic unit cell ($5\sqrt{3} \times 5\sqrt{3}$, $\angle = 60/120^o$) composed of two triangular, centrosymmetric half-unit cells. The half-unit cells of the discussed phase are linked by two aligned parallel molecules **A**, being a part of the three-fold coordination nodes **A_2BM** (top-left inset in Fig. 4). Additionally, the coordinatively saturated metal atoms embedded within a metal-organic network F_2 create an irregular 1-uniform 3.4.6.4 tessellation (see Fig. S2a of the Supplementary Data). The above mentioned pattern is called irregular because, in contrast to the 3.4.6.4 semi-regular Archimedean tiling, it is composed of a regular hexagon (side length 3), an equilateral triangle (side length $2\sqrt{3}$), and a rectangle ($3 \times 2\sqrt{3}$), instead of a square. As it follows from the visual inspection of a defect-free phase F_2, the *para*-functionalized linkers **B** present in its half-unit cells have identical molecular surroundings but are rotated by an angle of 60° with respect to each other. Moreover, the flower-like overlayer F_2 comprise two types of nanopores with different size and shape - hexagonal nanopores α (characteristic for the honeycomb-like network F_1) and unique voids δ encompassing 10 empty adsorption sites, each. On the other hand, the homologous phase F_3 is composed of two types of mononuclear coordination nodes **A_2BM** and **AB_2M**, differing in the stoichiometric ratio between linkers **A** and **B** (see the bottom-right part of Fig. 4). The centrosymmetric half-unit cells of a multilevel phase F_3 ($\rho_3 = 0.424$) make up a relatively large rhombic unit cell ($7\sqrt{3} \times 7\sqrt{3}$, $\angle = 60/120^o$) with diagonals equal to $e = 7\sqrt{3}$ and $g = e\sqrt{3}$, respectively (black intersecting arrows in the bottom-left inset in Fig. 4). Moreover, the metal atoms cementing coordination nodes of the stoichiometric network F_3 create an irregular 2-uniform 3.4.6.4; $3^3.4^2$ tessellation (the *k*-uniform tessellation has *k* types of distinct vertices and is composed of two or more types of regular polygons connected

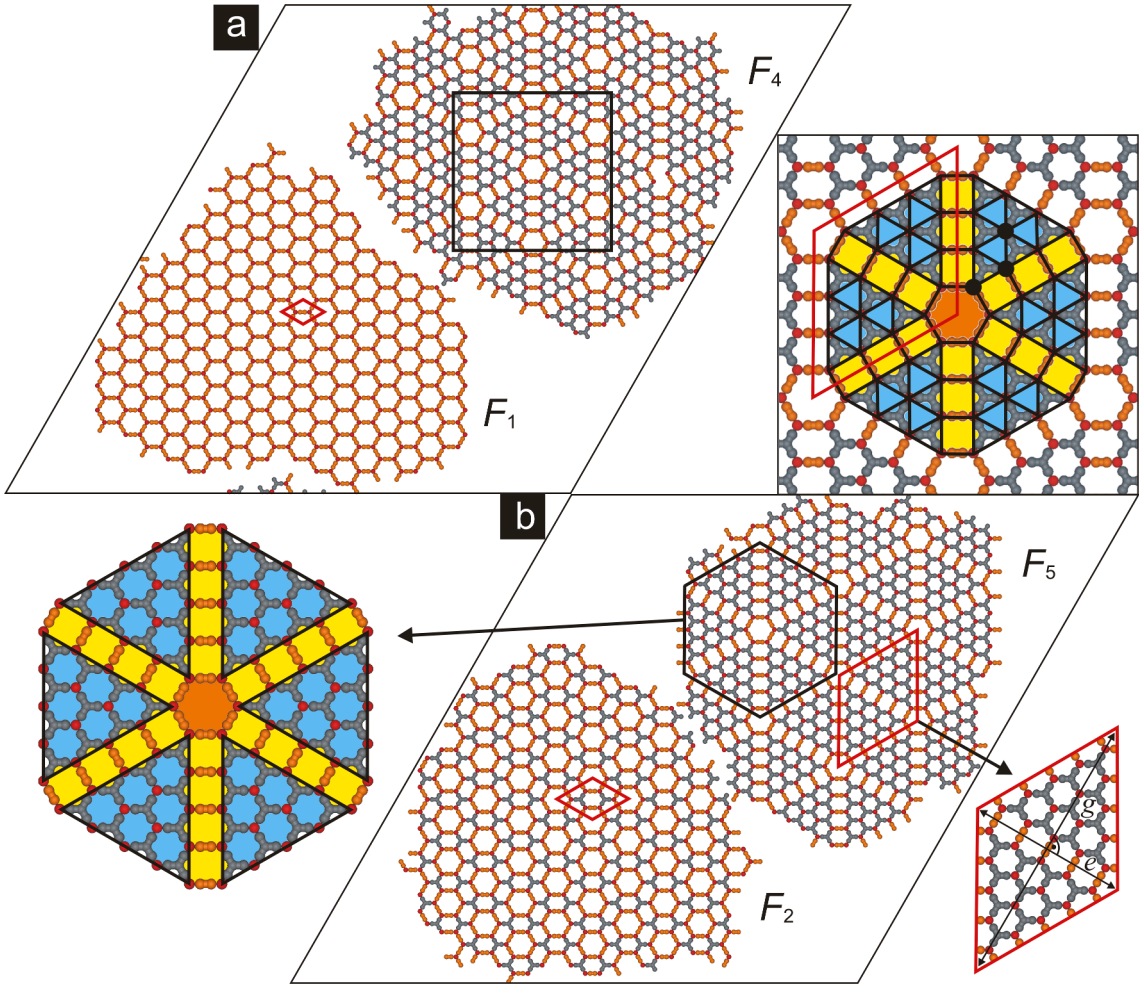

Fig. 5. The coexistence of flower-like metal-organic networks differing in structural index *n*. (a) Adsorbed overlayer comprising 762 linkers **A**, 254 molecules **B** and 762 metal atoms **M** in a ∼ 3 : 1 : 3 stoichiometric ratio. The solid black lines connecting the neighboring metal atoms in the magnified fragment of phase F_4 represent a fragment of an irregular 3-uniform 3.4.6.4; $3^3.4^2$; 3^6 tessellation, while the black dots indicate defining vertex points. The rhombic unit cells of separate nanoporous networks are marked by solid red lines. (b) Metal-organic overlayer composed of 550 linkers **A** 368 molecules **B** and 734 metal atoms **M** in a ∼ 3 : 2 : 4 stoichiometric ratio. The bottom-left inset presents a magnified hexagonal rosette r_5, the center of which is nanopore α (orange color) surrounded by concentrically arranged cavities β (light blue color) and δ (yellow color). The bottom-right inset presents a magnified rhombic unit cell of phase F_5 with marked perpendicular diagonals $e = 11\sqrt{3}$ and $g = e\sqrt{3}$.

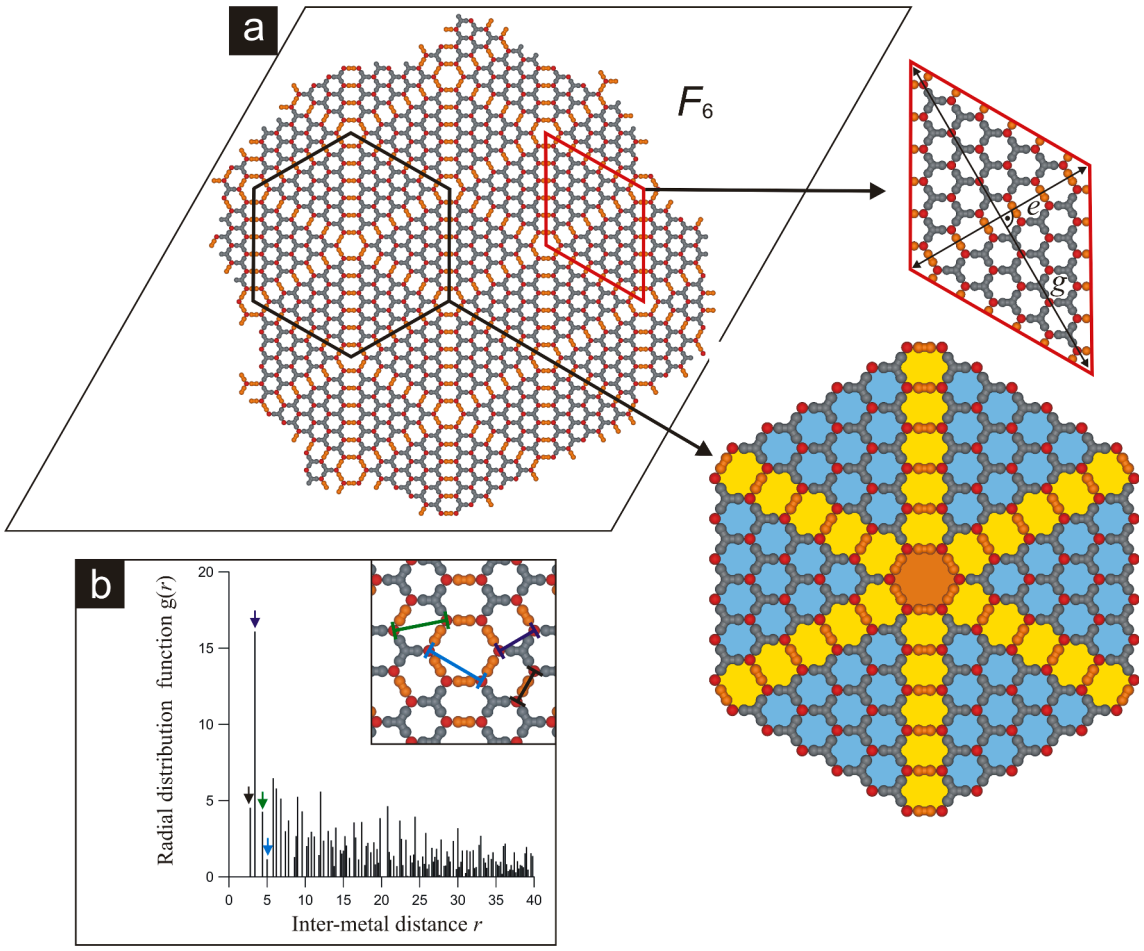

Fig. 6. (a) A representative snapshot of the achiral metal-organic network F_6 comprising 354 linkers **A** (orange rods), 472 molecules **B** (gray tripods) and 708 trivalent metal atoms **M** (red segments) in a $\sim$ 3 : 4 : 6 stoichiometric ratio. The solid red line delimits a rhombic unit cell with marked perpendicular diagonals ($e = 13\sqrt{3}$, $g = e\sqrt{3}$). The bottom-right inset presents a magnified hexagonal rosette, the center of which is nanopore α (orange color) surrounded by concentrically arranged cavities β (light blue color) and δ (yellow color). (b) Metal-metal radial distribution function $g(r)$ calculated for the flower-like network F_6 at temperature $T = 0.01$. Selected intermetallic distances **M**↔**M** are marked with different colors (black, purple, green, and light blue) and correspond to individual peaks (metal-metal coordination shells) of the metal-metal radial distribution function (color arrows).

edge-to-edge and vertex-to-vertex in the Euclidean plane),[45] built of the same polygons as the overlayer F_2 (for more details see Fig. S2b of the Supplementary Data). However, the continuous superstructure F_3 exhibits higher pore-type heterogeneity because it is composed of additional cavities β (7 adsorption sites), which are characteristic morphological feature of the homoporous network F_∞ (see Fig. 3a). The crystallinity of the comparing phases is confirmed by the corresponding metal-metal radial distribution functions $g(r)$ shown in Fig. 4c. Both $g(r)$ are composed of distinct, sharp peaks (metal-metal coordination shells) with fluctuating intensities. At large distances r, the individual peaks merge with one another and gradually decrease. However, at distance $r < 10$ their positions, number and relative intensities can be easily linked with structural properties of the homologous phases F_2 and F_3 (see insets in Fig. 4c). For example, the second peak ($r = 2\sqrt{3}$) is much higher for network F_3, what is associated with the elongation of the interpore distance d(α↔α). On the other hand, the fourth peak ($r = 3\sqrt{3}$) remarkably loses its intensity due to the less relative content of the hexagonal nanopores α within phase F_3 (see also Fig. 6b).

Importantly, the metal-assisted coassembly of linkers **A** and **B** can also lead to the formation of coexisting metal-organic phases with different morphology. Such complex structure formation is a common feature of reported so far hierarchically organized molecular assemblies, sustained by the weak intermolecular interactions [37–44], and the discussed herein metal-organic connections are no exception. Interestingly, in the theoretically studied molecular systems comprising *para*-functionalized ligands (**A** and **B**) we have never observed their complete separation and coexistence of the homoporous phases F_1 and F_∞ with extreme values of the structural index n. Namely, the self-assembly processes always resulted in the formation of individual extended overlayers (Figs. 4 and 6a) or coexistence of metal-organic networks differing in the value of structural index n (see Figs. 5 and S3 of the Supplementary Data). It means that among factors directing assembly of such complex patterns (surface coverage θ, composition of the adsorbed overlayer, temperature T, etc.) prominent role plays entropy of mixing.

Like in the case of low-structural index phases the topological properties of successive hierarchical networks F_n (where $n \geq 4$) also change in a highly systematic, predictable way. For example, within the openwork network F_4 ($\rho_4 = 0.437$), the periodically distributed hexagonal nanopores α are interconnected by the molecular ladders with steps formed by equispaced linkers **A** (**A**↔**A** $= 2\sqrt{3}$), while the coordinatively saturated metal atoms create an irregular 3-uniform 3.4.6.4; $3^3.4^2$; 3^6 tessellation (for more details see a magnified fragment of Fig. 5a). Moreover, a characteristic feature of any flower-like heteroporous phase F_n ($1 < n < \infty$) are achiral rosettes comprising $3(n^2 - n)$ tripod molecules **B** and $6T_n$ trivalent metal atoms **M**, where $T_n = 2^{-1}(n^2 + n)$ is a n-th triangular number, each (see the insets in Figs. 5 and 6). Each hexagonal rosette r_n is built of central nanopore α and six triangular domains

separated by molecular ladders composed of aligned parallel rod-like linkers **A**. The edges of a single triangular domain are composed of n evenly distributed three-fold coordination nodes $\mathbf{AB_2M}$, its vertices are nodal motifs $\mathbf{A_2BM}$, while $T_n - 3(n-1)$ elementary coordination nodes $\mathbf{B_3M}$ fill its interior. Moreover, the adjacent triangular domains belonging to a single rosette r_n are rotated by an angle of 60° with respect to each other.

The gradually increasing content of the tripod ligands **B** in the simulated metal-organic mixtures can lead also to the selective formation of extended high-structural index phases like those shown in Fig. 6a. The openwork superstructure F_6 ($\rho_6 = 0.451$) is composed of the huge achiral hexagonal rosettes r_6 (bottom-right inset in Fig. 6), and characterized by a rhombic unit cell ($13\sqrt{3} \times 13\sqrt{3}$, $\angle = 60/120°$). Like in the case of previously discussed overlayers ($n < 6$), the metal atoms embedded inside of a defect-free network F_6 are periodically distributed and create repetitive lace-like pattern. The high structural integrity of the above mentioned overlayer is also confirmed by the metal-metal radial distribution function $g(r)$, the diagram of which is shown in Fig. 6b. Among many peaks corresponding to the subsequent metal-metal coordination shells of the multilevel phase F_6, the most intense is the second peak ($r = 2\sqrt{3}$). This observation can be easily explained based on the structural analysis of a giant rosette r_6 shown in the bottom-right inset in Fig. 6. Namely, its triangular domains comprise exclusively interconnected three-fold coordination motifs $\mathbf{B_3M}$ with intermetallic distance **M**↔**M** equal to $2\sqrt{3}$. In general, the relative intensity of the second peak is strongly correlated with the size of triangular domains building hexagonal rosettes of any homologous phase F_n, and systematically increase with structural index n. On the other hand, the relative intensity of the fourth peak ($r = 3\sqrt{3}$) in diagram 6b is correlated with the total number of nanopores α (hexagonal rosettes r_6) present within the superstructure F_6, and systematically decrease with n. Therefore, in the case of infinite phase F_∞, the radial distribution peak located at $r = 3\sqrt{3}$ is equal to zero (see Fig. 3c).

To conclude, based on the scalable properties of the successive metal-organic phases F_n (where $n = 1, 2, 3, \ldots$), their morphology (porosity, connectivity, density ρ, composition of the unit cell, etc.) can be described in detail using structural index n. Namely, the rhombic unit cell of an arbitrary selected supramolecular network F_n consists of two adjacent triangular subunits (half-unit cells), has side length equal to $a_n = d_n(\alpha \leftrightarrow \alpha) = \sqrt{3}(2n+1)$ and contains a precisely defined number of trivalent metal atoms **M**, rod-like linkers **A**, and/or star-shaped molecules **B**. The length of the shorter diagonal e of a rhombic unit cell of phase F_n is equal to its side length $e_n = a_n$, while the longer one takes value $g_n = \sqrt{3}e_n$. Therefore, the total area A of a rhombic unit cell of any

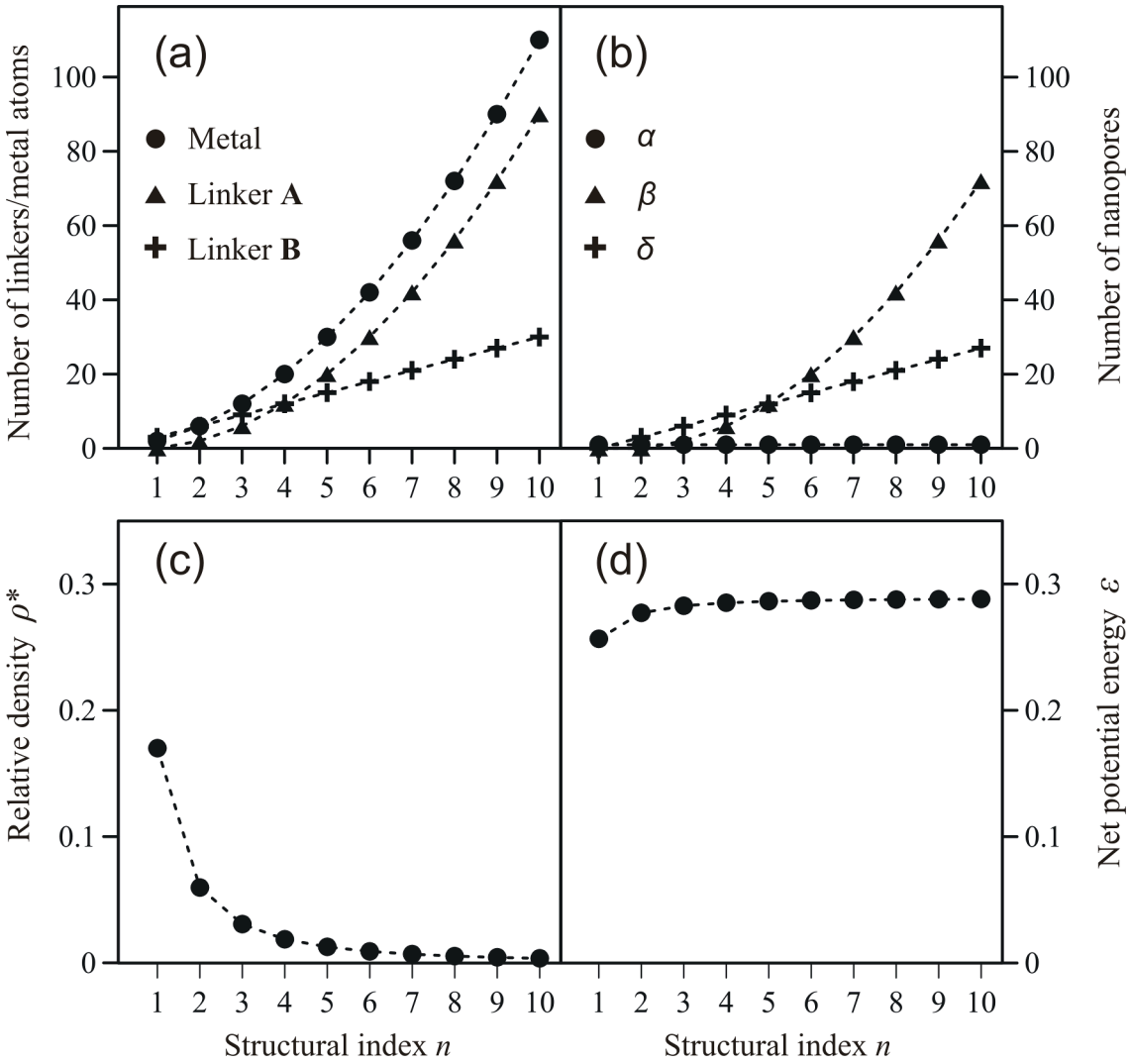

Fig. 7. The influence of the structural index n, where $1 \le n \le 10$ on (a) the total number of trivalent metal atoms **M** and bridging linkers (**A** and **B**) in a unit cell of phase F_n, (b) the total number of nanopores α, β and δ in a unit cell of phase F_n, (c) the relative density ρ* of the successive networks F_n and (d) the absolute value of the net potential energy ε per unit cell area A of the supramolecular network F_n.

phase F_n can be written as a discrete function of the structural index $A_n = 2^{-1}\sqrt{3}a_n^2$. The total number of trivalent metal atoms in a unit cell of superstructure F_n is a doubled sum of the subsequent natural numbers from 1 to n, that is $\mathbf{M}_n = n^2 + n$. A very similar relation is also true for the total number of tritopic molecules **B** present in a unit cell of periodic network F_n, namely $\mathbf{B}_n = n^2 - n$. The total number of linkers **A** in a rhombic unit cell of phase F_n scale linearly with the structural index $\mathbf{A}_n = 3n$ (see Fig. 7a). Therefore, the stoichiometric ratio between the components present in a unit cell of network F_n is equal to $\mathbf{M}_n$: $\mathbf{B}_n$: $\mathbf{A}_n = (n^2 + n)$: $(n^2 - n)$: $3n$. As it follows from this relationship, the molar ratios between bridging linkers **B** and **A** present in the rhombic unit cells of consecutive superstructures F_n, make up an infinite arithmetic progression with the initial term equal to zero and a common difference r between successive terms equal to $r = 3^{-1}$. Due to the hierarchical structure of the homologous overlayers F_n, the total number and type of empty nanopores (α, β, and δ) present in their unit cells are also correlated with the structural index n. Namely, the total number of hexagonal nanopores α within a unit cell of phase F_n is constant $\alpha_n = 1$, the total number of nanopores β is described by a quadratic equation $\beta_n = n^2 - 3n + 2$, while the total number of empty cavities δ is a linear function of the structural index $\delta_n = 3n - 3$ (see Fig. 7b). Therefore, the total number of nanopores present in a unit cell of phase F_n is equal to the square of the structural index $\alpha_n + \beta_n + \delta_n = n^2$ (additional morphology-structural index relationships of multilevel phases F_n are given in section 3. of the Supplementary Data). Based on the determined dependencies it is also possible to calculate the total number of free $f_n = 7n^2 + 9n + 3$ and occupied $\sigma_n = 5n^2 + 3n$ adsorption sites in a rhombic unit cell of the arbitrary selected hierarchical phase. Therefore, the density ρ of open porous phase F_n can be written as a discrete function of the structural index n in the following way $\rho_n = 2\sigma_n[\sqrt{3}\ a_n^2]^{-1}$. It means that the density ρ of the hierarchically organized metal-organic phases is a monotonically increasing function of a structural index n, that is $\rho_n = 2(5n^2+3n)[3\sqrt{3}(4n^2 + 4n + 1)]^{-1}$ (for more details see section 3.3 of the Supplementary Data). The asymptotical analysis of this equation leads to the conclusion that the lowest density ρ corresponds to the single-walled network F_1 ($\rho_1 = 0.342$), while for the very large values of the structural index ($n \to \infty$), the density of homologous assemblies asymptotically tends to the value, which is characteristic for a homoporous network F_∞ ($\rho_\infty = 0.481$). The next parameter, which allowed us to get a better insight into the structural properties of the flower-like phases F_n, is a relative density ρ*, defined in the following way:

$$\rho_n^* = \frac{\rho_{n+1} - \rho_n}{\rho_n} = \frac{8n^2 + 18n + 8}{20n^4 + 72n^3 + 81n^2 + 27n}$$

where ρ_n and ρ_{n+1} are densities of the consecutive networks F_n and F_{n+1}. As it is shown in Fig. 7c, their relative density ρ* decreases rapidly as n grows. Moreover, only the first few openwork phases differ significantly in terms of relative density ρ*, and for $n > 6$ the differences are almost negligible. In this context, the selective formation of a single metal-organic network F_n with desirable value of structural index n becomes more difficult when n grows. This conclusion remains in accordance with the results of previous studies devoted to the surface-assisted formation of multilevel assemblies [37,55,56].

Interestingly, as a discrete function of the structural index n, can also be written fraction ϕ of the occupied adsorption sites in a unit cell of any open porous phase F_n, that is

$$\varphi_n = \frac{\sigma_n}{\sigma_n + f_n} = \frac{5n^2 + 3n}{12n^2 + 12n + 3}$$

where σ_n stands for the number of occupied adsorption sites and f_n means the number of free (unoccupied) adsorption sites within a corresponding unit cell. Moreover, the parameter ϕ calculated for any metal-organic network belonging to the homologous series F_n a can be linked with its density, that is $\varphi_n = 2^{-1}\sqrt{3}\rho_n$. Therefore, the extreme values of fraction ϕ can be easily calculated: $\lim_{n\to 1}\varphi_n = 0.296$, and $\lim_{n\to\infty}\varphi_n = 0.417$. Besides the morphological properties of the achiral multilevel phases, we also analyzed the energy-related aspects associated with their spontaneous formation. Namely, the total number of anisotropic ligand → metal coordinate bonds in a unit cell of the metal-organic phase F_n is a quadratic function of structural index n, that is $3n^2 + 3n$. Therefore, the net potential energy ε per unit cell area of the superstructure F_n is equal to $\varepsilon_n = 2\omega(n^2 + n)[\sqrt{3}(4n^2 + 4n + 1)]^{-1}$, where $\omega = -1.0$ is the potential energy of a single ligand → metal coordinate bond (see Fig. 7d). Based on the asymptotical analysis of this formula, it is clear that, among an infinite series of hierarchically organized overlayers, the highest value of the absolute net potential energy ε per unit cell area corresponds to the homoporous network F_∞ (Fig. 3a), for which $\varepsilon_\infty = 0.289|\omega|$. On the other hand, the least value of the absolute net potential energy ε corresponds to a honeycomb-like phase F_1 (see Fig. 2a), for which the following relation $\varepsilon_1 = 0.889\varepsilon_\infty$ is true.

3.3. Chiral heteroporous metal-organic networks

Encouraged by the results obtained for organometallic mixtures described in the previous section, we performed additional calculations for the adsorbed overlayers comprising prochiral linkers **C**, trivalent metal atoms **M** and *para*-functionalized molecules **A'** with a linear backbone (**A'** = **A** + one collinear segment). As we demonstrated in our previous study the rod-like linkers **A'** mixed with trivalent metal atoms are able to assemble into ordered 2D nanomesh with spacious hexagonal cavities [57] (see also Fig. S4 of the Supplementary Data). Therefore, we expected that the metal-directed self-assembly of rod-like molecules **A'** and prochiral molecules **C** could result not only in the formation a family of flower-like metal-organic networks but also in the spontaneous induction of their chirality. Importantly, our speculations have confirmed the results of MC computer simulations. Namely, in the three-component mixtures composed of achiral linkers **A'**, conformationally flexible ligands **C** and trivalent metal atoms **M** we observed the formation a series of chiral polymorphic phases F_n' (see Figs. 8 and S5 of the Supplementary Data), where n is the structural index, defined as the total number of equidistant linkers **A'**, perpendicular to the line segment connecting the centers of the neighboring nanopores α′ present within network F_n'.

As illustrated in Fig. 8a, the (R)-chiral overlayer F_2' ($\rho_2' = 0.397$) is characterized by a rhombic unit cell ($\sqrt{93} \times \sqrt{93}$, $\angle = 60/120^\circ$) composed of two triangular, centrosymmetric half-unit cells. A characteristic feature of the above mentioned superstructure are hexagonal rosettes r_2' build of centrally located nanopore α′ (37 adsorption sites) and six adjacent empty voids λ (8 adsorption sites), each. The metal atoms embedded within continuous metal-organic network F_2' are involved in the stabilization of three-fold coordination nodes **A'**$_2$(*rrr*)**CM** and create regular 2D pattern (see magnified fragment of Fig. 8a). The shown in Fig. 8b polymorphic phase F_3' ($\rho_3' = 0.399$) shares structural features characteristic to the open porous network F_2' like modular composition, size/shape of nanopores α′ and λ, and multi-walled arrangement of bridging linkers **A'** (the metal-organic overlayers F_2' and F_3' with the opposite chirality are shown in Fig. S5 of the Supplementary Data). However, its chirality is more expressed due to larger content of windmill-like conformers (*rrr*)**C**. Additionally, the globally chiral superstructure F_3' is cemented by two types of three-fold coordination nodes **A'**$_2$(*rrr*)**CM** and **A'**(*rrr*)**C**$_2$**M** (differing in the stoichiometric ratio between bridging linkers) and comprise additional star-shaped nanopores γ (4 adsorption sites), located at vertices of hexagonal nanopores α′.

As it is seen in Fig. 8c the high structural coherence of hierarchically organized overlayers F_2' and F_3' is confirmed by calculations of the corresponding metal-metal radial distribution functions $g(r)$. Diagrams of g

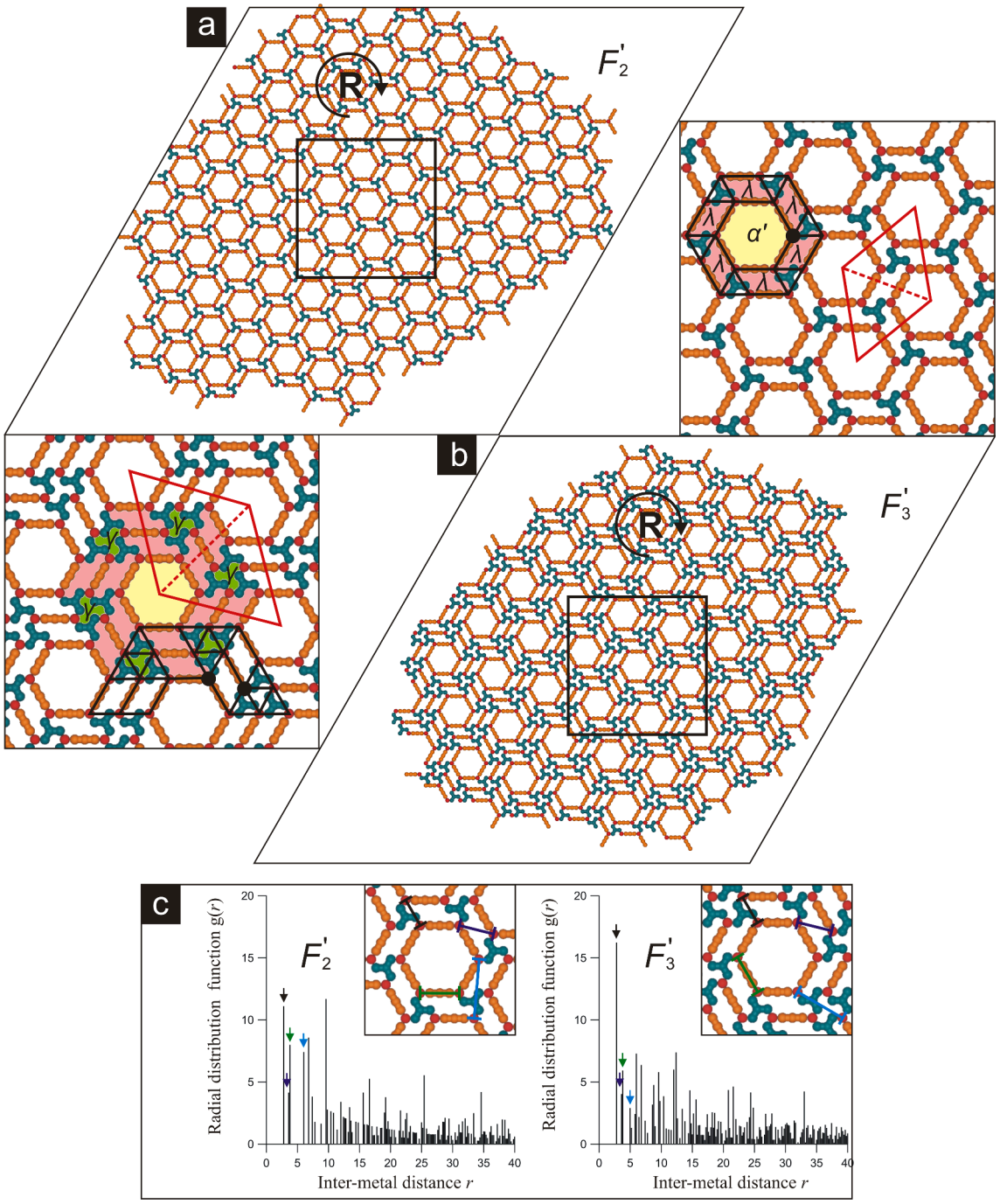

Fig. 8. (a) A representative snapshot of the (R)-chiral metal-organic network F_2' comprising 621 linkers **A'**, 207 conformers (*rrr*)**C** and 621 metal atom **M** in a 3: 1: 3 stoichiometric ratio. (b) The (R)-chiral phase F_3' comprising 474 linkers **A'**, 316 conformers (*rrr*)**C** and 632 metal atoms **M** in a $\sim$ 3 : 2 : 4 stoichiometric ratio. In the magnified fragments of the heteroporous networks, the rhombic unit cells are marked (solid red lines). The dashed red lines delimit triangular half-unit cells. The periodicity of the metal-organic phases is highlighted by the differently colored nanopores: α′ (chalk color), γ (pale green color) and λ (pink color). The solid black lines connecting the neighboring metal atoms in the magnified fragments of the multi-walled networks represent small fragments of the irregular 1-uniform 3.4.6.4 and the irregular 2-uniform 3.4.6.4; $3^3.4^2$ tessellation, while the black dots indicate defining vertex points. (c) Comparison of the metal-metal radial distribution functions $g(r)$ calculated for the successive networks F_2' and F_3' at temperature $T = 0.01$. Selected intermetallic distances **M**↔**M** are marked with different colors (black, purple, green, and light blue) and correspond to the individual peaks of the metal-metal radial distribution functions (color arrows).

(r) determined for the compared metal-organic phases are composed of distinct peaks with fluctuating (but gradually decreasing) intensities what is a clear manifestation of their crystalline structure.

The results presented in this section show clearly that the metal-assisted self-assembly of rod-like linkers **A'** and prochiral ligands **C** can lead to the formation a series of chiral networks with scalable topological properties like composition, connectivity, density ρ, nanopore spatial distribution, ect. As it follows from Figs. 8 and S6 of the Supplementary Data, the nanopore type, size and shape remains constant, regardless of the structural index n of metal-organic phase F_n' ($1 < n < \infty$), whereas the interpore distance $d(\alpha' \leftrightarrow \alpha')$ increases linearly with n. In consequence, when n decreases the chirality of homologous phases F_n' is gradually less expressed and it finally vanishes at $n = 1$ (see Fig. S4 of the Supplementary Data). In this context, the co(existence) of homologous

supramolecular architectures made up of the same building blocks but with significantly different morphology is possible in the discussed adsorbed systems (see Fig. S6 of the Supplementary Data). Moreover, the results of conducted MC simulations demonstrate that the conformationally flexible molecule **C** can be successfully used as a simple prochiral agent inducing chirality in the mixed metal-organic overlayers and offer a practical guide for rational fabrication of globally chiral SMONs (nanopatterned homochiral surfaces) with potential application in chiral catalysis and enantioselective separation/recognition of organic species.

4. Conclusions

In summary, we theoretically demonstrated that the metal-directed coassembly of archetypical π aromatic ligands with distinct symmetries and different number of active centers (functional groups) can results in the spontaneous formation a family of openwork metal-organic architectures with high structural complexity. Particularly, we observed the coordination-driven self-assembly a homologous series of topologically non-trivial SMONs with a hierarchical structure, controllable chirality, and scalable morphological properties. The structure-related parameters of the obtained supramolecular architectures were determined algebraically as discrete functions of structural index $n \in N$. Moreover, their crystallinity was confirmed by the metal-metal radial distribution function $g(r)$ calculations. The modeled supramolecular networks are not only aesthetically pleasing but also important for cognitive reasons. Namely, the mononuclear metal centers incorporated into their structure are arranged into non-trivial 2D tessellations (periodic mosaics) and thus realize fundamental mathematical ideas of Euclidean geometry. Furthermore, the real existence of the simulated flower-like SMONs can be verified by the appropriately designed STM experiments in UHV environment (for example with the use of easily accessible pyridine ligands **A**(**A'**)-**C**, trivalent Fe/Co atoms and atomically smooth metallic substrates with 111 geometry). Moreover, we hypothesise that the surface-assisted coassembly of halogenated derivatives of molecular bricks used in our study (**A** and **B**, where G = Br, I), can results in the formation a cascade of multilevel halogen-bonded 2D networks isostructural to those presented in our study. The comprehensive computational investigations devoted to such exotic molecular assemblies are ongoing in our laboratory.

Declaration of Competing Interest

The authors declare that they have no known competing financial interests or personal relationships that could have appeared to influence the work reported in this paper.

Acknowledgments

This work was supported by the National Science Centre, Poland [grant number: 2018/31/D/ST4/01443, SONATA 14].

Supplementary materials

Supplementary material associated with this article can be found, in the online version, at doi:10.1016/j.susc.2022.122041.

References

[1] L. Dong, Z. Gao, N. Lin, Self-assembly of metal-organic coordination structures on surfaces, Progr. Surf. Sci. 91 (2016) 101–135, https://doi.org/10.1016/j.progsurf.2016.08.001, https://doi.org/.
[2] Y. Wakayama, On-surface molecular nanoarchitectonics: from self-assembly to directed assembly, Jpn. J. Appl. Phys. 55 (2016) 1102AA, https://doi.org/10.7567/JJAP.55.1102AA, https://doi.org/.
[3] J.V. Barth, Fresh perspectives for surface coordination chemistry, Surf. Sci. 603 (2009) 1533–1541, https://doi.org/10.1016/j.susc.2008.09.049, https://doi.org/.
[4] U. Schlickum, F. Klappenberger, R. Decker, G. Zoppellaro, S. Klyatskaya, M. Ruben, K. Kern, H. Brune, J.V. Barth, Surface-confined metal-organic nanostructures from Co-directed assembly of linear terphenyl-dicarbonitrile linkers on Ag(111), J. Phys. Chem. C 114 (2010) 15602–15606, https://doi.org/10.1021/jp104518h, https://doi.org/.
[5] R. Adhikari, J. Kuliga, M. Ruppel, N. Jux, H. Marbach, H.P. Steinrück, Self-assembled 2D-coordination Kagome, quadratic, and close-packed hexagonal lattices formed from a cyano-functionalized benzoporphyrin on Cu(111), J. Phys. Chem. C 125 (2021) 7204–7212, https://doi.org/10.1021/acs.jpcc.1c00746, https://doi.org/.
[6] Y. Song, Y. Wang, Q. Jin, K. Zhou, Z. Shi, P.N. Liu, Y. Ma, Self-assembly and local manipulation of Au-pyridyl coordination networks on metal surfaces, ChemPhysChem 18 (2017) 2088–2093, https://doi.org/10.1002/cphc.201700439, https://doi.org/.
[7] J. Liu, J. Li, Z. Xu, X. Zhou, Q. Xue, T. Wu, M. Zhong, R. Li, R. Sun, Z. Shen, H. Tang, S. Gao, B. Wang, S. Hou, Y. Wang, On-surface preparation of coordinated lanthanide-transition-metal clusters, Nat. Commun. 12 (2021) 1619, https://doi.org/10.1038/s41467-021-21911-z, https://doi.org/.
[8] L. Yan, B. Xia, Q. Zhang, G. Kuang, H. Xu, J. Liu, P.N. Liu, N. Lin, Stabilizing and organizing Bi_3Cu_4 and Bi_7Cu_{12} nanoclusters in two-dimensional metal-organic networks, Angew. Chem. Int. Ed. 57 (2018) 4617–4621, https://doi.org/10.1002/anie.201800906, https://doi.org/.
[9] D. Moreno, B. Cirera, S.O. Parreiras, J.I. Urgel, N. Giménez-Agulló, K. Lauwaet, J. M. Gallego, J.R. Galán-Mascarós, J.I. Martínez, P. Ballester, R. Miranda, D. Écija, Dysprosium-directed metallosupramolecular network on graphene/Ir(111), Chem. Commun. 57 (2021) 1380–1383, https://doi.org/10.1039/D0CC07315F, https://doi.org/.
[10] M. Lischka, G.S. Michelitsch, N. Martsinovich, J. Eichhorn, A. Rastgoo-Lahrood, T. Strunskus, R. Breuer, K. Reuter, M. Schmittel, M. Lackinger, Remote functionalization in surface-assisted dehalogenation by conformational mechanics: organometallic self-assembly of 3,3′,5,5′-tetrabromo-2,2′,4,4′,6,6′-hexafluorobiphenyl on Ag(111), Nanoscale 10 (2018) 12035–12044, https://doi.org/10.1039/C8NR01987H, https://doi.org/.
[11] J.I. Urgel, D. Ecija, W. Auwärter, J.V. Barth, Controlled manipulation of gadolinium-coordinated supramolecules by low-temperature scanning tunneling microscopy, Nano Lett 14 (2014) 1369–1373, https://doi.org/10.1021/nl4044339, https://doi.org/.
[12] Z. Chen, S. Klyatskaya, J.I. Urgel, D. Écija, O. Fuhr, W. Auwärter, J.V. Barth, M. Ruben, Synthesis, characterization, monolayer assembly and 2D lanthanide coordination of a linear terphenyl-di(propiolonitrile) linker on Ag(111), Beilstein J. Nanotechnol. 6 (2015) 327–335, https://doi.org/10.3762/bjnano.6.31, https://doi.org/.
[13] X. Zhang, N. Li, L. Liu, G. Gu, C. Li, H. Tang, L. Peng, S. Hou, Y. Wang, Robust Sierpiński triangle fractals on symmetry-mismatched Ag(100), Chem. Commun. 52 (2016) 10578–10581, https://doi.org/10.1039/C6CC04879J, https://doi.org/.
[14] J.I. Urgel, B. Cirera, Y. Wang, W. Auwärter, R. Otero, J.M. Gallego, M. Alcamí, S. Klyatskaya, M. Ruben, F. Martín, R. Miranda, D. Ecija, J.V. Barth, Surface-supported robust 2D lanthanide-carboxylate coordination networks, Small 11 (2015) 6358–6364, https://doi.org/10.1002/smll.201502761, https://doi.org/.
[15] L. Song, B. Yang, F. Liu, K. Niu, Y. Han, J. Wang, Y. Zheng, H. Zhang, Q. Li, L. Chi, Synthesis of two-dimensional metal-organic frameworks via dehydrogenation reactions on a Cu(111) surface, J. Phys. Chem. C 124 (2020) 12390–12396, https://doi.org/10.1021/acs.jpcc.0c00931, https://doi.org/.
[16] M.A. Dubois, O. Guillermet, S. Gauthier, G. Zhan, Y. Makoudi, F. Palmino, X. Bouju, A. Rochefort, Influence of Cu adatoms on the molecular assembly of 4,4′-bipyridine on Cu(111), Phys. Chem. Chem. Phys. 20 (2018) 15350–15357, https://doi.org/10.1039/C8CP01184B, https://doi.org/.
[17] U. Schlickum, R. Decker, F. Klappenberger, G. Zoppellaro, S. Klyatskaya, M. Ruben, Silanes I, A. Arnau, K. Kern, H. Brune, J.V. Barth, Metal-organic honeycomb nanomeshes with tunable Cavity size, Nano Lett 7 (2007) 3813–3817, https://doi.org/10.1021/nl072466m, https://doi.org/.
[18] B.D. Baker Cortés, N. Schmidt, M. Enache, M. Stöhr, Comparing cyanophenyl and pyridyl ligands in the formation of porphyrin-based metal-organic coordination networks, J. Phys. Chem. C 125 (2021) 24557–24567, https://doi.org/10.1021/acs.jpcc.1c05360, https://doi.org/.
[19] R. Zhang, G. Lyu, C. Chen, T. Lin, J. Liu, P.N. Liu, N. Lin, Two-dimensional superlattices of Bi nanoclusters formed on a Au(111) surface using porous supramolecular templates, ACS Nano 9 (2015) 8547–8553, https://doi.org/10.1021/acsnano.5b03676, https://doi.org/.
[20] R. Gutzler, S. Stepanow, D. Grumelli, M. Lingenfelder, K. Kern, Mimicking enzymatic active sites on surfaces for energy conversion chemistry, Acc. Chem. Res. 48 (2015) 2132–2139, https://doi.org/10.1021/acs.accounts.5b00172, https://doi.org/.
[21] M. Pivetta, G.E. Pacchioni, U. Schlickum, J.V. Barth, H. Brune, Formation of Fe cluster superlattice in a metal-organic quantum-box network, Phys. Rev. Lett. 10 (2013), 086102, https://doi.org/10.1103/PhysRevLett.110.086102 https://doi.org/.
[22] K. Müller, M. Enache, M. Stöhr, Confinement properties of 2D porous molecular networks on metal surfaces, J. Phys.: Condens. Matter 28 (2016), 153003, https://doi.org/10.1088/0953-8984/28/15/153003 https://doi.org/.
[23] Q. Zhong, X. Li, H. Zhang, L. Chi, Noncontact atomic force microscopy: bond imaging and beyond, Surf. Sci. Rep. 75 (2020), 100509, https://doi.org/10.1016/j.surfrep.2020.100509 https://doi.org/.
[24] Y.F. Geng, P. Li, J.Z. Li, X.M. Zhang, Q.D. Zeng, C. Wang, STM probing the supramolecular coordination chemistry on solid surface: structure, dynamic, and

reactivity, Coord. Chem. Rev. 337 (2017) 145–177, https://doi.org/10.1016/j.ccr.2017.01.014, https://doi.org/.
[25] Y. Zhang, X. Zhang, Y. Li, S. Zhao, S. Hou, K. Wu, Y. Wang, Packing Sierpiński triangles into two-dimensional crystals, J. Am. Chem. Soc. 142 (2020) 17928–17932, https://doi.org/10.1021/jacs.0c08979, https://doi.org/.
[26] J.I. Urgel, D. Écija, G. Lyu, R. Zhang, C.A. Palma, W. Auwärter, N. Lin, J.V. Barth, Quasicrystallinity expressed in two-dimensional coordination networks, Nat. Chem. 8 (2016) 657–662, https://doi.org/10.1038/nchem.2507, https://doi.org/.
[27] Q. Sun, L. Cai, H. Ma, C. Yuan, W. Xu, On-surface construction of a metal-organic Sierpiński triangle, Chem. Commun. 51 (2015) 14164–14166, https://doi.org/10.1039/C5CC05554G, https://doi.org/.
[28] C. Li, X. Zhang, N. Li, Y. Wang, J. Yang, G. Gu, Y. Zhang, S. Hou, L. Peng, K. Wu, D. Nieckarz, P. Szabelski, H. Tang, Y. Wang, Construction of Sierpiński triangles up to the fifth order, J. Am. Chem. Soc. 139 (2017) 13749–13753, https://doi.org/10.1021/jacs.7b05720, https://doi.org/.
[29] D. Ecija, M. Marschall, J. Reichert, A. Kasperski, D. Nieckarz, P. Szabelski, W. Auwärter, J.V. Barth, Dynamics and thermal stability of surface-confined metal-organic chains, Surf. Sci. 643 (2016) 91–97, https://doi.org/10.1016/j.susc.2015.08.013, https://doi.org/.
[30] M. Ammon, T. Sander, S. Maier, On-surface synthesis of porous carbon nanoribbons from polymer chains, J. Am. Chem. Soc. 139 (2017) 12976–12984, https://doi.org/10.1021/jacs.7b04783, https://doi.org/.
[31] T. Nijs, Y.M. Klein, S.F. Mousavi, A. Ahsan, S. Nowakowska, E.C. Constable, C. E. Housecroft, T.A. Jung, The different faces of 4′-pyrimidinyl functionalized 4,2′:6′,4′′-terpyridines: metal organic assemblies from solution and on Au(111) and Cu (111) surface platforms, J. Am. Chem. Soc. 140 (2018) 2933–2939, https://doi.org/10.1021/jacs.7b12624, https://doi.org/.
[32] X. Zhang, Q. Shen, H. Ding, X. Chen, H. Yang, B. Li, X. Liu, H. Lin, Q. Li, J. Gao, G. Li, M. Pan, Q. Guo, On-surface synthesis of thiophene-containing large-sized organometallic macrocycles on the Ag(111) surface, J. Phys. Chem. C 125 (2021) 11454–11461, https://doi.org/10.1021/acs.jpcc.1c01540, https://doi.org/.
[33] Q. Fan, C. Wang, Y. Han, J. Zhu, J. Kuttner, G. Hilt, J.M. Gottfried, Surface-assisted formation, assembly, and dynamics of planar organometallic macrocycles and zigzag shaped polymer chains with C-Cu-C bonds, ACS Nano 8 (2014) 709–718, https://doi.org/10.1021/nn405370s, https://doi.org/.
[34] M. Marschall, J. Reichert, A. Weber-Bargioni, K. Seufert, W. Auwärter, S. Klyatskaya, G. Zoppellaro, M. Ruben, J.V. Barth, Random two-dimensional string networks based on divergent coordination assembly, Nat. Chem. 2 (2010) 131–137, https://doi.org/10.1038/nchem.503, https://doi.org/.
[35] J. Liu, T. Lin, Z. Shi, F. Xia, L. Dong, P.N. Liu, N. Lin, Structural transformation of two-dimensional metal-organic coordination networks driven by intrinsic in-plane compression, J. Am. Chem. Soc. 133 (2011) 18760–18766, https://doi.org/10.1021/ja2056193, https://doi.org/.
[36] Y. Ye, W. Sun, Y. Wang, X. Shao, X. Xu, F. Cheng, J. Li, K. Wu, A unified model: self-assembly of trimesic acid on gold, J. Phys. Chem. C 111 (2007) 10138–10141, https://doi.org/10.1021/jp072726o, https://doi.org/.
[37] W. Xiao, X. Feng, P. Ruffieux, O. Gröning, K. Müllen, R. Fasel, Self-assembly of chiral molecular honeycomb networks on Au(111), J. Am. Chem. Soc. 130 (2008) 8910–8912, https://doi.org/10.1021/ja7106542, https://doi.org/.
[38] T. Jasper-Tönnies, M. Gruber, S. Ulrich, R. Herges, R. Berndt, Coverage-controlled superstructures of C_3-symmetric molecules: honeycomb versus hexagonal tiling, Angew. Chem. Int. Ed. 59 (2020) 7008–7017, https://doi.org/10.1002/anie.202001383, https://doi.org/.
[39] J. Zhang, B. Li, X. Cui, B. Wang, J. Yang, J.G. Hou, Spontaneous chiral resolution in supramolecular assembly of 2,4,6-tris(2-pyridyl)-1,3,5-triazine on Au(111), J. Am. Chem. Soc. 131 (2009) 5885–5890, https://doi.org/10.1021/ja9001986, https://doi.org/.
[40] L.M. Wang, J.Y. Yue, Q.Y. Zheng, D. Wang, Temperature-directed hierarchical surface supramolecular assembly, J. Phys. Chem. C 123 (2019) 13775–13781, https://doi.org/10.1021/acs.jpcc.9b03545, https://doi.org/.
[41] S. Clair, M. Abel, L. Porte, Mesoscopic arrays from supramolecular self-assembly, Angew. Chem. Int. Ed. 49 (2010) 8237–8239, https://doi.org/10.1002/anie.201003335, https://doi.org/.
[42] S.S Jester, E. Sigmund, L.M. Röck, S. Höger, Hierarchical self-assembly of polycyclic heteroaromatic stars into snowflake patterns, Angew. Chem. Int. Ed. 124 (2012) 1–6, https://doi.org/10.1002/anie.201204006, https://doi.org/.
[43] C. Liu, Y. Yu, W. Zhang, Q. Zeng, S. Lei, Room-temperature synthesis of covalent organic frameworks with a boronic ester linkage at the liquid/solid interface, Chem. Eur. J. 22 (2016) 18412–18418, https://doi.org/10.1002/chem.201603547, https://doi.org/.
[44] J. Liu, T. Chen, X. Deng, D. Wang, J. Pei, L.J. Wan, Chiral hierarchical molecular nanostructures on two-dimensional surface by controllable trinary self-assembly, J. Am. Chem. Soc. 133 (2011) 21010–21015, https://doi.org/10.1021/ja209469d, https://doi.org/.
[45] D. Nieckarz, P. Szabelski, Simulation of the self-assembly of simple molecular bricks into Sierpiński triangles, Chem. Commun. 50 (2014) 6843–6845, https://doi.org/10.1039/C4CC01344A, https://doi.org/.
[46] J. Lisiecki, P. Szabelski, Surface-confined metal-organic precursors comprising naphthalene-like derivatives with differently distributed halogen substituents: a Monte Carlo model, J. Phys. Chem. C 124 (2020) 20280–20293, https://doi.org/10.1021/acs.jpcc.0c06726, https://doi.org/.
[47] F. Bischoff, Y. He, K. Seufert, D. Stassen, D. Bonifazi, J.V. Barth, W. Auwärter, Tailoring large pores of porphyrin networks on Ag(111) by metal-organic coordination, Chem. Eur. J. 22 (2016) 15298–15306, https://doi.org/10.1002/chem.201602154, https://doi.org/.
[48] N. Metropolis, A.W. Rosenbluth, M.N. Rosenbluth, A.H. Teller, Equation of state calculations by fast computing machines, J. Chem. Phys. 21 (1953) 1087–1092, https://doi.org/10.1063/1.1699114, https://doi.org/.
[49] A. Kumar, K. Banerjee, A.S. Foster, P. Liljeroth, Two-dimensional band structure in honeycomb metal-organic frameworks, Nano Lett 18 (2018) 5596–5602, https://doi.org/10.1021/acs.nanolett.8b02062, https://doi.org/.
[50] L. Cai, Q. Sun, M. Bao, H. Ma, C. Yuan, W. Xu, Competition between hydrogen bonds and coordination bonds steered by the surface molecular coverage, ACS Nano 11 (2017) 3727–3732, https://doi.org/10.1021/acsnano.6b08374, https://doi.org/.
[51] K. Gdula, D. Nieckarz, On-surface self-assembly of metal-organic architectures: insights from computer simulations, J. Phys. Chem. C 124 (2020) 20066–20078, https://doi.org/10.1021/acs.jpcc.0c04597, https://doi.org/.
[52] T.R. Umbach, M. Bernien, C.F. Hermanns, A. Krüger, V. Sessi, I. Fernandez-Torrente, P. Stoll, J.I. Pascual, K.J. Franke, W. Kuch, Ferromagnetic coupling of mononuclear Fe centers in a self-assembled metal-organic network on Au(111), Phys. Rev. Lett. 109 (2012) 267, https://doi.org/10.1103/PhysRevLett.109.267207. –207. https://doi.org/.
[53] Z. Shi, J. Liu, T. Lin, F. Xia, P.N. Liu, N. Lin, Thermodynamics and selectivity of two-dimensional metallo-supramolecular self-assembly resolved at molecular scale, J. Am. Chem. Soc. 133 (2011) 6150–6153, https://doi.org/10.1021/ja2010434, https://doi.org/.
[54] D. Nieckarz, P. Szabelski, Self-assembly of conformationally flexible molecules under 2D confinement: structural analysis from computer simulations, Chem. Commun. 54 (2018) 8749–8752, https://doi.org/10.1039/C8CC04272A, https://doi.org/.
[55] A.I. Fadeeva, V.A. Gorbunov, O.S. Solovyeva, P.V. Stishenko, A.V. Myshlyavtsev, Homologous series of flower phases in metal-organic networks on Au(111) surface, J. Phys. Chem. C 124 (2020) 11506–11515, https://doi.org/10.1021/acs.jpcc.0c02527, https://doi.org/.
[56] W. Rżysko, D. Nieckarz, P. Szabelski, Hierarchical ordering in adsorbed overlayers of chiral tripod molecules with directional interactions, J. Phys. Chem. C 121 (2017) 410–420, https://doi.org/10.1021/acs.jpcc.6b10710, https://doi.org/.
[57] D. Nieckarz, P. Szabelski, Understanding pattern formation in 2D metal-organic coordination systems on solid surfaces, J. Phys. Chem. C 117 (2013) 11229–11241, https://doi.org/10.1021/jp4022486, https://doi.org/.